ELSEVIER

Volume 181, Number 6, June 2008

JOURNAL OF SOLID STATE CHEMISTRY

www.elsevier.com/locate/jssc

CONTENTS

Abstracted/indexed in BioEngineering Abstracts, Chemical Abstracts, Coal Abstracts, Current Contents/Physics, Chemical, & Earth Sciences, Engineering Index, Research Alert, SCISEARCH, Science Abstracts, and Science Citation Index. Also covered in the abstract and citation database SCOPUS®. Full text available on ScienceDirect®.

Regular Articles

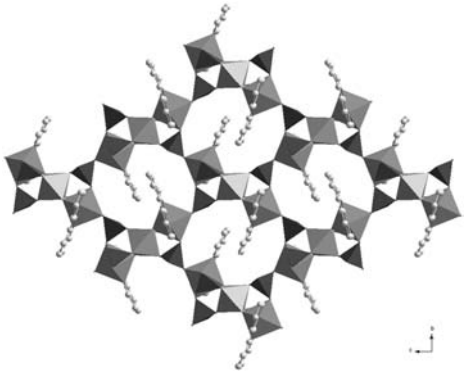

The first two-dimensional layer gallium phosphite $Ga_3F_2(2,2'\text{-bipy})_2(HPO_3)_2(H_{1.5}PO_3)_2$ with 10-membered ring windows along the *a*-axis, which is built from the novel heptameric building unit.

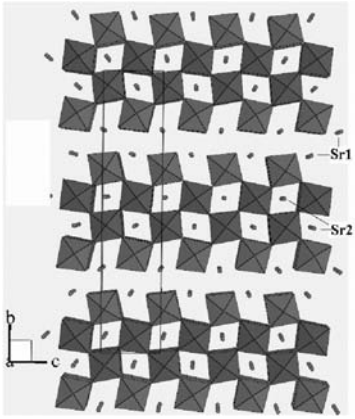

Layered crystal structure of $Sr_2Nb_2O_7$.

Regular Articles—Continued

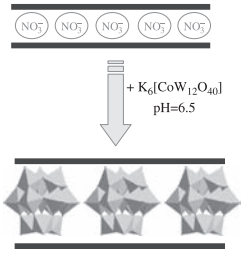

A tungstocobaltate anion $[CoW_{12}O_{40}]^{5-}$ pillared layered double hydroxide (LDH) was prepared by aqueous ion exchange with a Mg-Al LDH precursor in nitrate form, demonstrating that $[CoW_{12}O_{40}]^{5-}$ was intercalated between the brucite-type layers of the LDHs without change in structure. Magnetic measurement shows the occurrence of antiferromagnetic interactions between the magnetic centers. The investigation of catalytic performance for this sample exhibits high activity for the oxidation of benzaldehyde by hydrogen peroxide.

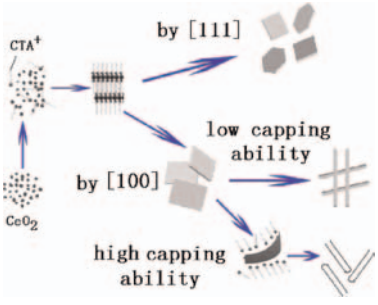

CeO_2 nanoplates were synthesized by hydrothermal reactions assisted by CTAB, and the controlled conversion of nanoplates into nanotubes, and nanorods were realized by changing the CTAB/Ce^{3+} ratio value, reaction time, and temperature. An excellent catalytic activity is found for CO oxidation using CeO_2 nanoplates due to their exposed surface (100).

Formation mechanism and luminescence appearance of Mn-doped zinc silicate particles synthesized in supercritical water
Masafumi Takesue, Atsuko Suino, Yukiya Hakuta, Hiromichi Hayashi and Richard Lee Smith Jr.
page 1307

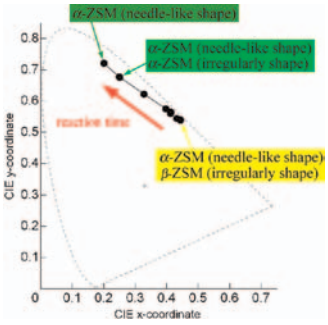

Luminescence appearance of Mn-doped zinc silicate (Zn_2SiO_4:Mn^{2+}, ZSM) formed in supercritical water at 400 °C and 29 MPa were studied in the relation to its phase formation mechanism. Green emission by α-ZSM and yellow emission by β-ZSM occurred over the same time period during the onset of phase formation.

The $Sr_{2.75}Ce_{0.25}Co_2O_{7-\delta}$ oxide, $n = 2$ member of the Ruddlesden–Popper series: Structural and magnetic evolution depending on oxygen stoichiometry
A. Demont, S. Hébert, D. Pelloquin and A. Maignan
page 1314

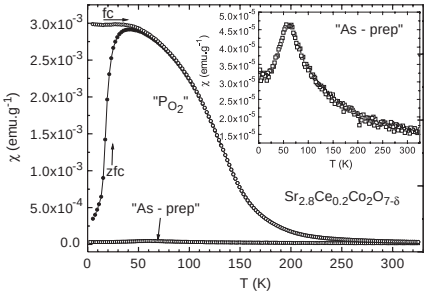

Temperature dependence of the magnetic susceptibility of as-prepared and PO_2 annealing $Sr_{2.75}Ce_{0.25}Co_2O_{7-\delta}$ RP2-type structures.

Structural and electrical properties of the $2Bi_2O_3 \cdot 3ZrO_2$ system
Čedomir Jovalekić, Miodrag Zdujić, Dejan Poleti, Ljiljana Karanović and Miodrag Mitrić
page 1321

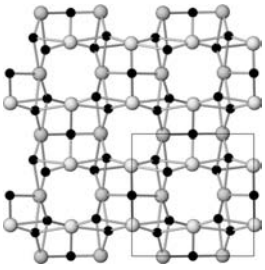

Powder mixtures of the $2Bi_2O_3 \cdot 3ZrO_2$ composition were thermally and mechanochemically treated in order to examine the obtained phases, which were characterized by DSC, electrical measurements, SEM, TEM, as well as X-ray and neutron powder diffraction. It is shown that resulting ZrO_2-doped β-Bi_2O_3 phase possess ferroelectric properties.

Synthesis, structure and magnetic behaviour of mixed metal leucophosphite
Fa-Nian Shi, António Moreira dos Santos, Luís Cunha-Silva, Benilde F.O. Costa, Jacek Klinowski, Filipe A. Almeida Paz, Vítor S. Amaral, João Rocha and Tito Trindade
page 1330

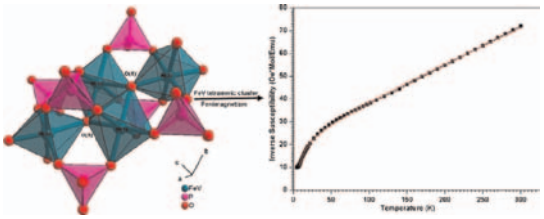

A new iron(III)–vanadium(III) phosphate, an analogue of leucophosphite, with chemical composition {K[(FeV)$(PO_4)_2$(OH)(H_2O)]$\cdot H_2O$}, was isolated using hydrothermal synthesis, and characterized structurally by single-crystal X-ray diffraction, thermogravimetric analysis and vibrational spectroscopy. The magnetic properties of the material show ferrimagnetic features at low temperature.

A potential red phosphor $ZnMoO_4$:Eu^{3+} for light-emitting diode application
Li-Ya Zhou, Jian-She Wei, Fu-Zhong Gong, Jun-Li Huang and Ling-Hong Yi
page 1337

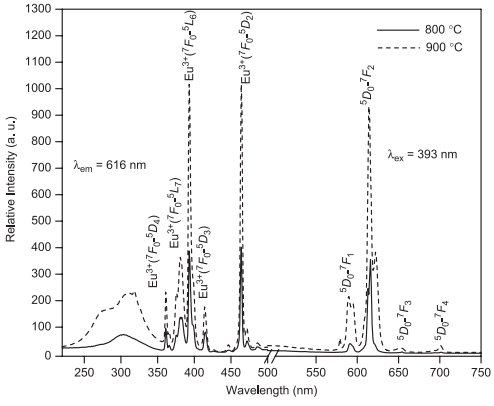

Motivated by the need for new red phosphors for solid-state lighting applications Eu^{3+}-doped $ZnMoO_4$ was prepared by solid-state reaction and its photoluminescence properties were investigated. Upon excitation with near UV light, the phosphor showed strong red-emission lines at around 616 nm and the optical properties study suggests that it is an efficient red-emitting phosphor for LED application.

Continued

Synthesis, crystal growth, and structure of Ta_3Al_2CoC—An ordered quarternary cubic η-carbide and the first single crystal study of a η-carbide

Johannes Etzkorn and Harald Hillebrecht

page 1342

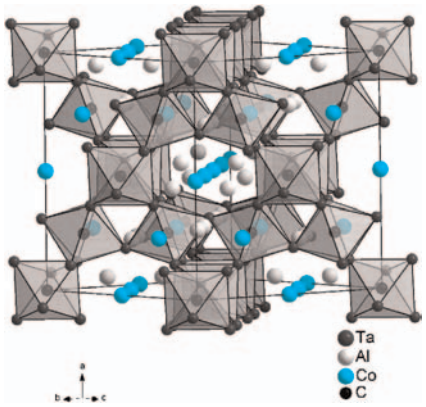

Single crystals of the η-carbide Ta_3Al_2CoC were grown from a Co-melt. Although η-carbides are technologically very important as a constituent of cermets this is the first report on a single crystal study. The structure analysis of this quarternary variant shows the close similarity to the Ni_2Ti-structure as an ordering and filling variant. All sites are completely occupied and well ordered.

Charge ordering and dielectric properties in the near half-doped $Pr_{0.79}Na_{0.21}MnO_3$ perovskite

M. Sánchez-Andújar, S. Yáñez-Vilar, S. Castro-García and M.A. Señarís-Rodríguez

page 1354

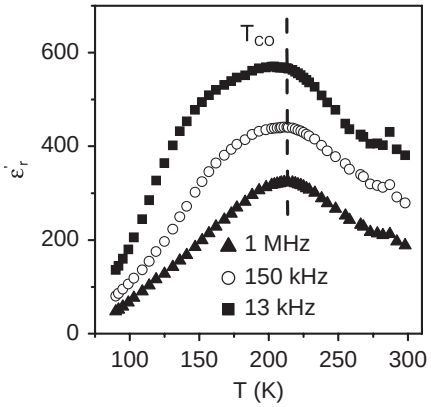

We have prepared the near half-doped $Pr_{0.79}Na_{0.21}MnO_3$ perovskite, whose SXRPD data can be refined both on the basis of the site-centred and bond-centred model in the CO state. Its dielectric constant shows an anomaly at T_{CO} whose origin is intrinsic and that we relate to the formation of polar entities at the temperature of charge condensation due to an asymmetric intermediate charge distribution.

Two isotypic diphosphates $LiM_2H_3(P_2O_7)_2$ (M = Ni, Co) containing ferromagnetic zigzag MO_6 chains

Tao Yang, Sihai Yang, Fuhui Liao and Jianhua Lin

page 1347

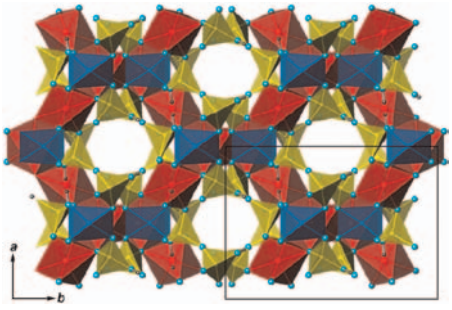

$LiNi_2H_3(P_2O_7)_2$ (**1**) and $LiCo_2H_3(P_2O_7)_2$ (**2**) have been hydrothermally synthesized and structurally characterized. The MO_6 octahedra share edges forming zigzag chains with P_2O_7 as the interchain groups. Both of them are quasi-one-dimensional magnets and have ferromagnetic MO_6 chains; **1** is a ferromagnet, whereas **2** is a metamagnet.

Photocatalytic degradation of organic dyes on visible-light responsive photocatalyst $PbBiO_2Br$

Zhichao Shan, Wendeng Wang, Xinping Lin, Hanming Ding and Fuqiang Huang

page 1361

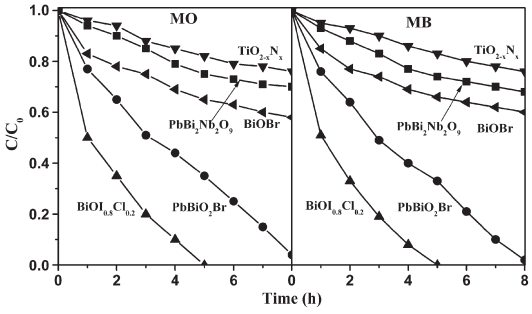

The as-prepared layered $PbBiO_2Br$ with an optical band gap of 2.3 eV possesses a fair visible-light-response ability. The references, $PbBi_2Nb_2O_9$, $TiO_{2-x}N_x$, BiOBr and $BiOI_{0.8}Cl_{0.2}$, were applied to comparatively understand the activity of $PbBiO_2Br$. Degradation of dyes was used to evaluate photocatalytic activity. The results show that $PbBiO_2Br$ is more photocatalytically active than $PbBi_2Nb_2O_9$, $TiO_{2-x}N_x$ and BiOBr under visible light.

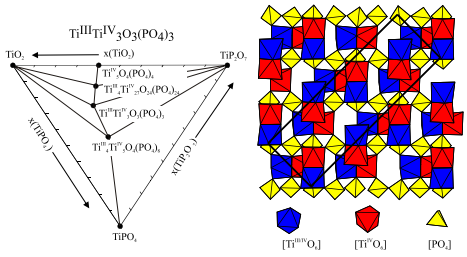

Single crystals of the oxidephosphates $Ti^{III}Ti^{IV}_3O_3(PO_4)_3$ (black), $Cr^{III}_4Ti^{IV}_{27}O_{24}(PO_4)_{24}$ (red-brown, transparent), and $Fe^{III}_4Ti^{IV}_{27}O_{24}(PO_4)_{24}$ (brown) with edge-lengths up to 0.3 mm were grown by chemical vapour transport. The crystal structures of these orthorhombic members of the lazulite/lipscombite structure family were refined from single-crystal data.

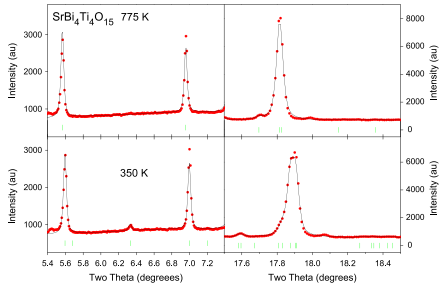

Synchrotron X-ray and neutron powder diffraction have been used to establish the temperature dependent structures of Aurivillius-type oxides of the type $ABi_4Ti_4O_{15}$.

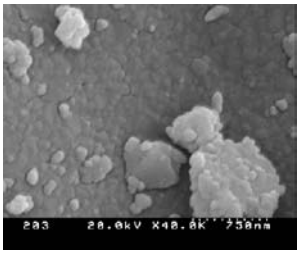

$LiAl_5O_8$:Eu^{3+} phosphors have been synthesized in a very short time (lt;5 min) by combustion process and are well characterized by XRD and SEM. TL glow peak was observed in gamma-irradiated Eu ion-doped $LiAl_5O_8$ at around 180 °C. Electron spin resonance studies have been carried out in order to study the characteristics of the defect centres. Photoluminescence studies showed red emission located at about 613 nm and is ascribed to $^5D_0$–$^7F_2$ transition of Eu^{3+} ions.

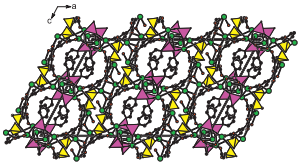

Three novel mixed-ligand lead(II) carboxylate–arsonates, namely, $Pb_5(SIP)_2(L^1)_2(H_2O)$ **1**, $Pb_3(SIP)(L^2)(H_2O)$ **2** and $Pb(H_2L^2)(H_2BTC)$ **3** have been synthesized and structurally characterized. Compounds **1** and **2** feature complicated 3D network structures whereas compound **3** features 1D lead(II) carboxylate–arsonate chains that are further interlinked by strong hydrogen bonds into a 3D supramolecular assembly.

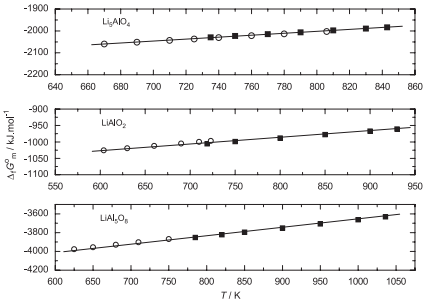

Comparison of $\Delta_f G^0_m$ of ternary oxides determined from KEQMS and solid-state galvanic cell techniques. (O) KEQMS, (■) solid-state galvanic cell and solid line: combined fit of both the experimental data.

Compared to other zirconium phosphates, α-$Zr_2O(PO_4)_2$ shows a remarkable low thermal expansion of $2.6 \times 10^{-6} K^{-1}$.

Continued

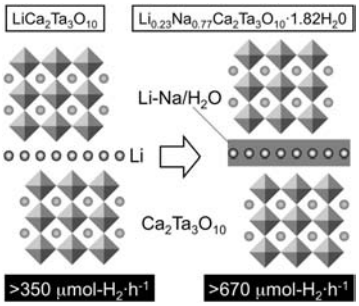

The partial substitution of Na in the interlayer of anhydrous-layered perovskite has been found as useful structural modification toward highly active hydrated photocatalysts.

Mixed conductivity, oxygen permeability and redox behavior of K_2NiF_4-type $La_2Ni_{0.9}Fe_{0.1}O_{4+\delta}$

V.V. Kharton, E.V. Tsipis, E.N. Naumovich, A. Thursfield, M.V. Patrakeev, V.A. Kolotygin, J.C. Waerenborgh and I.S. Metcalfe

page 1425

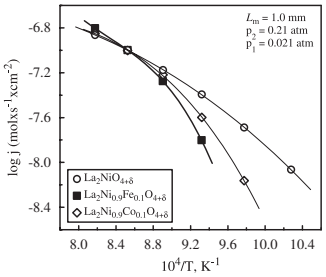

Oxygen permeation fluxes through iron-doped lanthanum nickelate ceramics.

Preparation and thermoelectric properties of $AgPb_mSbSe_{m+2}$ materials

K.F. Cai, X.R. He, M. Avdeev, D.H. Yu, J.L. Cui and H. Li

page 1434

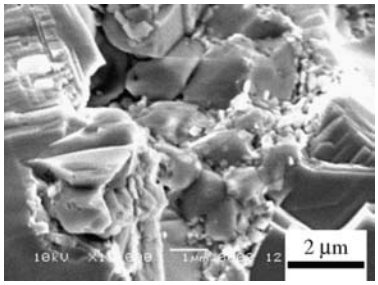

SEM image of the fracture surface of an $Ag_{0.85}Pb_{18}SbSe_{20}$ nano/micron composite material prepared by spark plasma sintering of hydrothermally synthesized nanopowders.

Rapid synthesis of tin (IV) oxide nanoparticles by microwave induced thermohydrolysis

J. Jouhannaud, J. Rossignol and D. Stuerga

page 1439

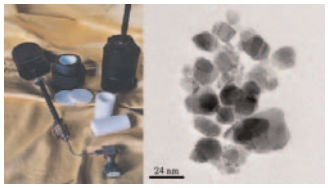

Tin oxide-based gas sensors have been extensively studied in recent years in order to understand and improve their sensing properties to a large variety of gaseous species. As is well known, high specific surface area increase the responses of gas sensors. Microwave-induced thermohydrolysis appears as an efficient way to produce nanoparticles in a very short time, with controlled size (4–5 nm) and high-specific area (160–190 $m^2\,g^{-1}$). Pictogram represents our original microwave reactor, the RAMO (French acronym of Réacteur Autoclave Micro-Onde), containing the reactants and submitted to the microwave irradiation (multicolour candy represent obtained material), and a typical TEM image of the as-prepared SnO_2 nanoparticles.

Structural characterisation of the $Ce_{1-x}La_xNbO_{4+\delta}$ solid solution series: *In-situ* high-temperature powder diffraction studies

R.J. Packer, P.A. Stuart and S.J. Skinner

page 1445

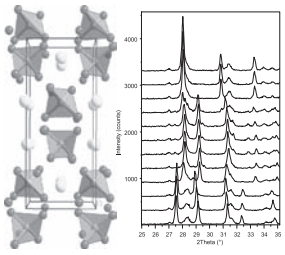

Tetragonal scheelite-type structure (left) and *in-situ* X-ray powder diffraction data highlighting the oxidation and phase transformation of end member $CeNbO_{4+\delta}$.

Fluorescence and phosphorescence properties of the low temperature forms of the $MAl_2Si_2O_8$:Eu^{2+} (M = Ca, Sr, Ba) compounds

Frédéric Clabau, Alain Garcia, Pierre Bonville, Danielle Gonbeau, Thierry Le Mercier, Philippe Deniard and Stéphane Jobic

page 1456

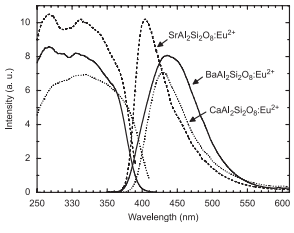

The Eu^{2+}-doped $MAl_2Si_2O_8$ (M = Ca, Sr, and Ba) aluminosilicates exhibit a bluish white luminescence, which can last several minutes after the removal of the excitation. The account for Eu^{2+} cations coupled with defects is required to explain fluorescence spectra.

Synthesis of homo and hetero metal-phosphonate frameworks from bi-functional aminomethylphosphonic acid

Christian R. Samanamu, Elena Nicole Zamora, Jean-Luc Montchamp and Anne F. Richards
page 1462

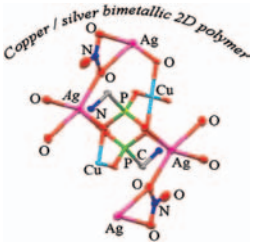

The synthesis and characterization of polymeric metal phosphonates featuring zinc, cadmium, mercury, lead, and silver phosphonate are described from the reactions of the bi-funtional aminomethylphosphonic acid with the metal precursor in aqueous conditions. These previously undescribed polymers display unusual structural features and include the synthesis of a bimetallic metal-organic framework (Cu/Ag).

Thermal expansion of $Cr_{2x}Fe_{2-2x}Mo_3O_{12}$, $Al_{2x}Fe_{2-2x}Mo_3O_{12}$ and $Al_{2x}Cr_{2-2x}Mo_3O_{12}$ solid solutions
M. Ari, P.M. Jardim, B.A. Marinkovic, F. Rizzo and F.F. Ferreira
page 1472

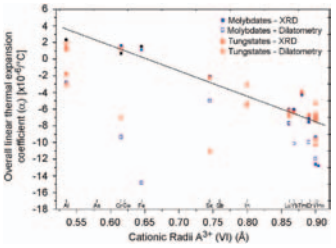

In this figure, all published overall linear coefficients of thermal expansion for orthorhombic $A_2M_3O_{12}$ family obtained through diffraction methods as a function of A^{3+} cation radii size, together with dilatometric results, are plotted. Our results indicate that $Cr_2Mo_3O_{12}$ does not exactly follow the established relationship.

Phase equilibria and crystal structure of the complex oxides in the Sr–Fe–Co–O system
T.V. Aksenova, L.Ya. Gavrilova and V.A. Cherepanov
page 1480

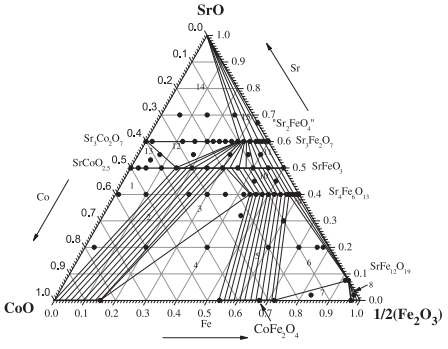

Isobaric–isothermal cross-section of phase diagram of the Sr–Fe–Co–O system at 1100 °C in air.

New anion-templated 3D heterobimetallic open frameworks based on lanthanide-carboxylate layers and copper pillars
Yun-Wu Li, Yong-Hui Wang, Yang-Guang Li and En-Bo Wang
page 1485

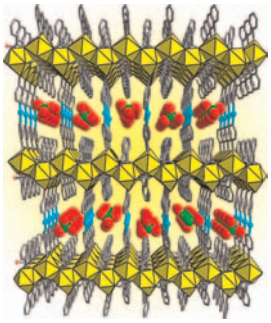

A series of new anion-templated 3D heterobimetallic open framework based on the lanthanide-carboxylate layers and copper(I)-inic pillars, $[Ln_2(1,2\text{-bdc})_2(H_2O)_2Cu(inic)_2](ClO_4)$ (Ln = Eu **(1)**, Tb **(2)**, Nd **(3)** and Sm **(4)**; 1,2-bdc = 1,2-benzenedicarboxylate; Hinic = isonicotinic acid), have been hydrothermally synthesized and structurally characterized, among which compounds **1** and **2** exhibit good fluorescent properties.

Anion substitution effects on the structure and magnetism of the chromium chalcogenide Cr_5Te_8—Part III: Structures and magnetism of the high-temperature modification $Cr_{(1+x)}Q_2$ and the low-temperature modification $Cr_{(5+x)}Q_8$ (Q = Te, Se; Te:Se = 5:3)
Joseph Wontcheu, Wolfgang Bensch, Sergiy Mankovsky, Svitlana Polesya, Hubert Ebert, Reinhard K. Kremer and Eva Brücher
page 1492

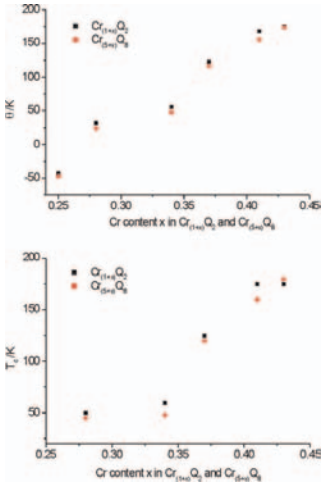

The magnetic properties of $Cr_{1+x}Q_2$ and $Cr_{5+x}Te_5Se_3$ (Q = Te, Se; ratio = 5:3) are strongly influenced by the Cr content and the crystal structure with the Weiss constant and Curie temperature covering a large range.

Continued

Author inquiries

Submissions

For detailed instructions on the preparation of electronic artwork, consult the journal home page at http://authors.elsevier.com.

Other inquiries

Visit the journal home page (http://authors.elsevier.com) for the facility to track accepted articles and set up e-mail alerts to inform you of when an article's status has changed. The journal home page also provides detailed artwork guidelines, copyright information, frequently asked questions and more.

Contact details for questions arising after acceptance of an article, especially those relating to proofs, are provided after registration of an article for publication.

Language Polishing

Authors who require information about language editing and copyediting services pre- and post-submission should visit http://www.elsevier.com/wps/find/authorshome.authors/languagepolishing or contact authorsupport@elsevier.com for more information. Please note Elsevier neither endorses nor takes responsibility for any products, goods, or services offered by outside vendors through our services or in any advertising. For more information please refer to our Terms & Conditions at http://www.elsevier.com/wps/find/termsconditions.cws_home/termsconditions.

For a full and complete Guide for Authors, please refer to *J. Solid State Chem.,* Vol. 180, Issue 1, pp. *bmi–bmv*. The instructions can also be found at http://www.elsevier.com/wps/find/journaldescription.cws_home/622898/authorinstructions.

Journal of Solid State Chemistry has no page charges.